

Synergizing Fe₂O₃ Nanoparticles on Single Atom Fe-N-C for Nitrate Reduction to Ammonia at Industrial Current Densities

Eamonn Murphy, Baiyu Sun, Martina Rüscher, Yuanchao Liu, Wenjie Zang, Shengyuan Guo, Yu-Han Chen, Uta Hejral, Ying Huang, Alvin Ly, Iryna V. Zenyuk, Xiaoqing Pan, Janis Timoshenko, Beatriz Roldán Cuenya, Erik D. Spoecke, and Plamen Atanassov*

The electrochemical reduction of nitrates (NO₃⁻) enables a pathway for the carbon neutral synthesis of ammonia (NH₃), via the nitrate reduction reaction (NO₃RR), which has been demonstrated at high selectivity. However, to make NH₃ synthesis cost-competitive with current technologies, high NH₃ partial current densities (*j*_{NH₃}) must be achieved to reduce the levelized cost of NH₃. Here, the high NO₃RR activity of Fe-based materials is leveraged to synthesize a novel active particle-active support system with Fe₂O₃ nanoparticles supported on atomically dispersed Fe-N-C. The optimized 3×Fe₂O₃/Fe-N-C catalyst demonstrates an ultrahigh NO₃RR activity, reaching a maximum *j*_{NH₃} of 1.95 A cm⁻² at a Faradaic efficiency (FE) for NH₃ of 100% and an NH₃ yield rate over 9 mmol hr⁻¹ cm⁻². Operando XANES and post-mortem XPS reveal the importance of a pre-reduction activation step, reducing the surface Fe₂O₃ (Fe³⁺) to highly active Fe⁰ sites, which are maintained during electrolysis. Durability studies demonstrate the robustness of both the Fe₂O₃ particles and Fe-N_x sites at highly cathodic potentials, maintaining a current of -1.3 A cm⁻² over 24 hours. This work exhibits an effective and durable active particle-active support system enhancing the performance of the NO₃RR, enabling industrially relevant current densities and near 100% selectivity.

1. Introduction

The synthesis of ammonia (NH₃) based fertilizers is essential to support the growing global food demands. Currently, thermochemical NH₃ synthesis via the Haber Bosch (HB) process, accounts for ≈2% of global energy usage and more than 1.4% of global CO₂ emissions.^[1-3] The electrochemical reduction of di-nitrogen (N₂) is a theoretically ideal NH₃ synthesis pathway, however, direct activation of the highly stable and insoluble (in protic electrolytes) N₂ molecule remains challenging and unproven.^[4,5] As an alternative for the N₂ molecule, recently there has been a revitalized interest in the more oxidized form of nitrogen, nitrate (NO₃⁻). Nitrate is an environmental pollutant present in groundwater runoffs due to heavy overfertilization practices and in industrial waste streams at varying concentrations (0.001–2 M).^[6,7] The reduction of NO₃⁻ to NH₃ is appealing

E. Murphy, B. Sun, Y. Liu, S. Guo, Y.-H. Chen, I. V. Zenyuk, P. Atanassov
Department of Chemical and Biomolecular Engineering
National Fuel Cell Research Center
University of California
Irvine, CA 92697, USA
E-mail: plamen.atanassov@uci.edu

M. Rüscher, U. Hejral, J. Timoshenko, B. R. Cuenya
Department of Interface Science
Fritz-Haber-Institut der Max-Planck-Gesellschaft
14195 Berlin, Germany

W. Zang, Y. Huang, A. Ly, X. Pan
Department of Materials Science and Engineering
University of California
Irvine, CA 92697, USA

E. D. Spoecke
Sandia National Laboratories, Energy Storage Technologies & Systems
Albuquerque, NM 87185, USA

The ORCID identification number(s) for the author(s) of this article can be found under <https://doi.org/10.1002/adma.202401133>

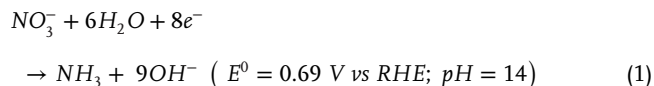
© 2024 The Authors. Advanced Materials published by Wiley-VCH GmbH. This is an open access article under the terms of the [Creative Commons Attribution-NonCommercial-NoDerivs](#) License, which permits use and distribution in any medium, provided the original work is properly cited, the use is non-commercial and no modifications or adaptations are made.

DOI: 10.1002/adma.202401133

to reutilize waste nitrogen into value-added NH_3 , alleviating the demand on the HB process, while also serving as an alternative to traditional denitrification techniques, providing dual benefits for the nitrate reduction reaction (NO_3RR). It should be noted that the NO_3RR alone is not a replacement for the HB process, because typically, the nitrogen atom in the NO_3^- originates from an HB-produced NH_3 , but the NO_3RR can help to enhance the efficiency of the N-cycle.^[8] Or the NO_3RR can be coupled with N_2 plasma oxidation processes to be totally decoupled from the HB process.

Electrochemically, the NO_3RR is a complex $8e^-$ transfer reaction, consisting of several possible soluble and insoluble intermediates (NO_2 , NO_2^- , NO , N_2 , N_2O , NH_2OH , NH_3 , and N_2H_4) and competes directly with the hydrogen evolution reaction (HER).^[9] Aiming at industrial relevance, it is essential to optimize both catalyst activity and selectivity towards a singular product, in this discussion, NH_3 . In practice, the use of an alkaline media (pH 13–14) can enhance the NO_3RR current throughput (over most metals) and significantly suppress the formation of the common $2e^-$ side product, nitrite (NO_2^-), often reporting the highest NH_3 Faradaic efficiencies (FE_{NH_3}) and yield rates ($Yield_{\text{NH}_3}$) as shown in Table S1, Supporting Information.^[10–14]

When targeting industrially relevant current densities, there is a competing compromise between the energy efficiency and NH_3 partial current density (j_{NH_3}), both of which are influenced by the applied cathodic potential and corresponding NH_3 selectivity. In alkaline media, the standard reduction potential for the NO_3RR to NH_3 (Equation (1)) is 0.69 V versus RHE.^[12,15]



Currently, several reports achieve high FE_{NH_3} pushing upwards of 90%, some at mildly reductive potentials, resulting in relatively high cathodic energy efficiencies, $\approx 40\%$.^[12,13,16–19] However, most of these reports suffer from limited j_{NH_3} ($0.5 - 100 \text{ mA cm}^{-2}$), resulting in the need for largely scaled-up devices or stacks and thus intensive capital costs of these systems. In contrast, the NO_3RR systems with higher j_{NH_3} ($100 < X \text{ mA cm}^{-2}$) relied on more cathodic overpotentials, suffering from largely reduced energy efficiencies (e.g., below 30%).^[11,20–22] Establishing a trade-off between energy efficiency and j_{NH_3} remains ambiguous, although, a recent economic analysis quantifying the leveled cost of NH_3 , suggested that the j_{NH_3} (production rate) has a more significant influence than the cell voltage or electricity price in reducing the leveled cost of NH_3 .^[22]

Cost-efficient platinum-group-metal-free (PGM-free) metals typically require more cathodic potentials to achieve a desirable j_{NH_3} . One way to achieve higher energy efficiency is to utilize PGMs and their alloys as these metals often have earlier (closer to the thermodynamic) reaction onset potentials. However, as more cathodic potentials are applied to achieve higher j_{NH_3} , they are typically out-competed by HER.^[13,23] However, due to their scarcity and price, large-scale systems based on PGMs are not economically feasible. A promising approach was recently demonstrated, utilizing a Cu nanowire decorated with atomically dispersed Ru, able to achieve current densities at over 90% FE_{NH_3} .^[10] Other recently reported rational strate-

gies involve employing bi-metallic systems to selectively tailor the N-intermediate binding energies or selectively invoke a cascade mechanism for highly selective NO_3^- to NH_3/N_2 conversion. It was shown that analogous to an approach utilized in the CO_2RR , pulsing cathodic and anodic potentials were shown to enhance NO_3RR by optimizing $^*\text{NO}$ adsorption, reaching over 97% FE_{NH_3} . Another possible strategy currently being investigated for the oxygen reduction reaction (ORR) is the use of active supports to increase the activity and durability of the catalyst systems.^[24–26] In those cases, a typical inert carbon support (Vulcan / carbon black) is replaced with an ORR active, atomically dispersed metal–nitrogen–carbon (M–N–C) support, often Fe–N–C or Co–N–C. It is speculated that possible electron donation between the platinum nanoparticles and the M–N–C can create more favorable intermediate adsorption energies, increasing the activity. Additionally, it was suggested that the M– N_4 active site can modify the electronic structure of the neighboring carbon, increasing the stability of the nanoparticles.

It has been shown in our previous works and complemented by other studies that atomically dispersed Fe–N–C is highly active for the NO_3RR , achieving a FE_{NH_3} greater than 90%.^[12,27–29] This work builds upon the high NO_3RR activity of Fe–N–C catalysts and utilizes it as an active-support for Fe_2O_3 nanoparticles, synthesizing a $\text{Fe}_2\text{O}_3/\text{Fe–N–C}$ system for ultra-high NO_3RR to NH_3 performance. Specifically, the $3\times\text{Fe}_2\text{O}_3/\text{Fe–N–C}$ catalyst exhibits a potential independent selectivity ($\approx 100\% FE_{\text{NH}_3}$) between -0.4 to -1.2 V versus RHE, while increasing the j_{NH_3} up to nearly 2 A cm^{-2} (at a $Yield_{\text{NH}_3}$ of more than $9 \text{ mmol}_{\text{NH}_3} \text{ h}^{-1} \text{ cm}^{-2}$). In situ X-ray absorption near edge structure (XANES) supported by post-mortem X-ray photoelectron spectroscopy (XPS) reveals that the pre-reduction activation step is critical in achieving the ultrahigh NO_3RR performance, generating highly active, surface Fe^0 sites. A durability test showed that the optimized $3\times\text{Fe}_2\text{O}_3/\text{Fe–N–C}$ catalyst could maintain a FE_{NH_3} between 90–100% at a current of 1.3 A cm^{-2} for over 24-h, demonstrating the durability of utilizing an active-catalyst/active-support system.

2. Results and Discussion

2.1. $\text{Fe}_2\text{O}_3/\text{Fe–N–C}$ Synthesis and Characterization

Fe_2O_3 nanoparticles supported on atomically dispersed Fe–N–C ($\text{Fe}_2\text{O}_3/\text{Fe–N–C}$) were synthesized by utilizing the sacrificial support method (SSM) for the Fe–N–C, followed by an organic solvent synthesis method for the Fe_2O_3 nanoparticles. The SSM is a robust technique developed by our group for the synthesis of atomically dispersed M–N–C catalysts.^[28] Schematically, the SSM is shown in Figure 1a, wherein a catalyst slurry of a carbon-nitrogen precursor is mixed with nanoporous silica and an iron-nitrate salt. The precursor mixture then undergoes a series of ball milling, pyrolyzing, and acid etching steps, yielding an exclusively atomically dispersed Fe–N–C support.^[28] Afterward, the Fe_2O_3 nanoparticles were synthesized on either a Vulcan-XC72 or Fe–N–C support, utilizing an organic solvent method. The high-angle annular dark-field scanning transmission electron microscopy (HAADF-STEM) image (Figure 1b) and TEM images (Figures S1 and S2, Supporting Information) show a homogeneous dispersion of the Fe_2O_3 nanoparticles with

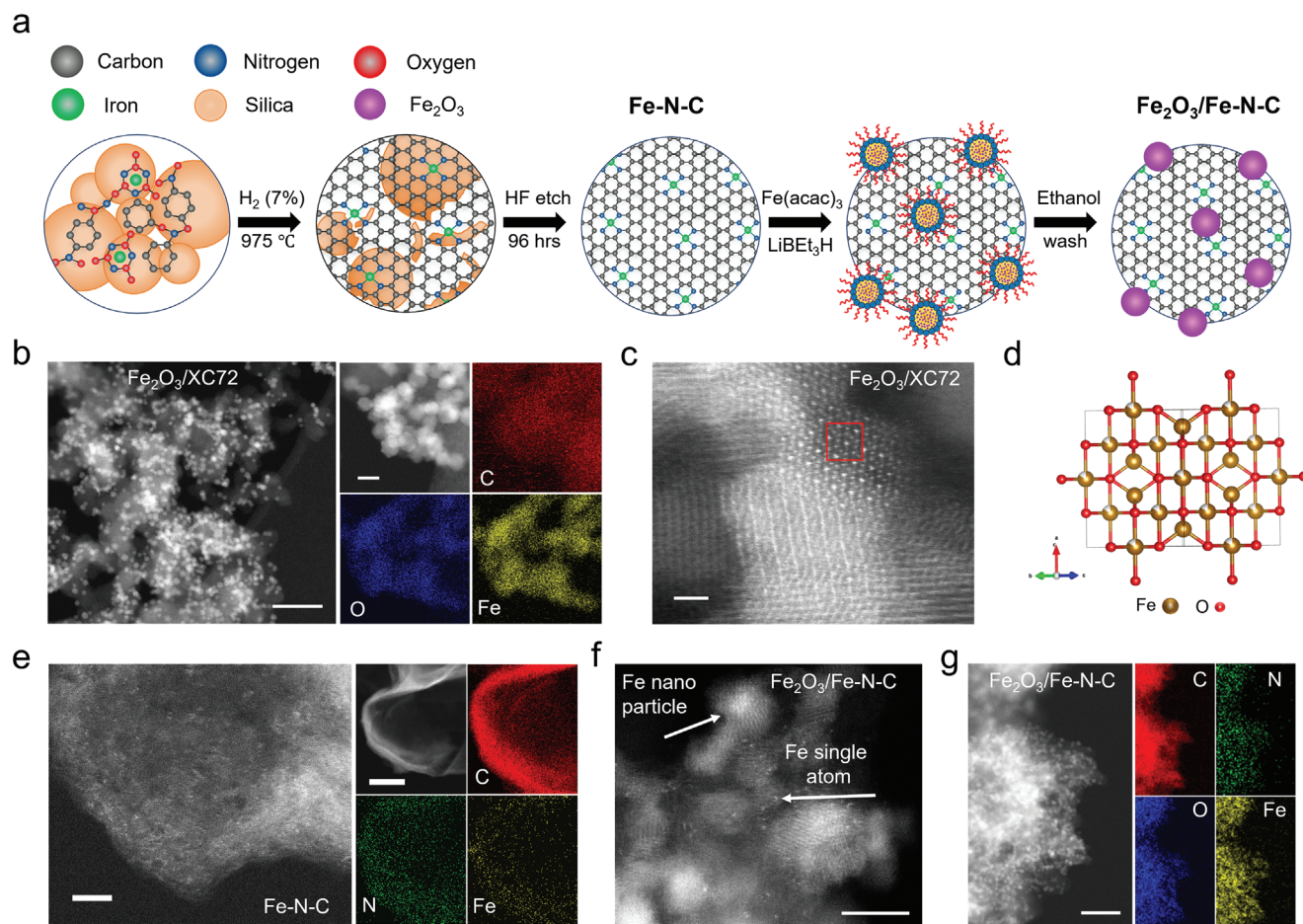


Figure 1. Synthesis schematic and AC-HAADF-STEM images of Fe_2O_3 -based catalysts. a) Synthesis schematic, utilizing the sacrificial support method and an organic solvent synthesis to deposit Fe_2O_3 nanoparticles on the atomically dispersed Fe–N–C. b) STEM images of the Fe_2O_3 catalyst supported on XC72 carbon, the scale bar is 50 nm, with its corresponding EDS mapping, scale bar is 5 nm. c) Atomic resolution STEM image showing the Fe_2O_3 spinel structure, scale bar is 2 nm. d) Schematic representation of the Fe_2O_3 spinel crystal structure, created using VESTA. e) Atomic resolution STEM image of the atomically dispersed Fe–N–C catalyst support, with its corresponding EDS mapping, scale bar is 2 nm. f) Atomic resolution STEM image showing the Fe_2O_3 nanoparticles supported on the atomically dispersed Fe–N–C, scale bar is 5 nm. g) EDS mapping of the $\text{Fe}_2\text{O}_3/\text{Fe-N-C}$ catalyst, scale bar is 50 nm.

well-controlled sub-5 nm diameter. Additionally, the corresponding elemental mapping is shown in Figure 1b, for the $\text{Fe}_2\text{O}_3/\text{XC72}$ catalyst with a homogeneous distribution of Fe, O, and C. The Fe_2O_3 nanoparticles have a spinel-like structure, typical of gamma-phase Fe_2O_3 , as observed in the HAADF-STEM image in Figure 1c. A schematic of the Fe_2O_3 spinel crystal structure is given in Figure 1d. The high magnification STEM image and energy dispersive X-ray spectroscopy (EDS) mapping in Figure 1e, verify the atomic dispersion of Fe and N-doping in the Fe–N–C support. After reducing the Fe_2O_3 nanoparticles onto the Fe–N–C support, Figure 1f confirms that the Fe–N–C support retains its atomic dispersion as single atom Fe sites, clearly co-existing with the Fe_2O_3 nanoparticles. The corresponding EDS mapping of the $\text{Fe}_2\text{O}_3/\text{Fe-N-C}$ catalyst in Figure 1g, confirms the presence of nitrogen from the Fe–N–C support. The crystal structure of the catalyst was examined by X-ray diffraction (XRD), confirming the formation of Fe_2O_3 (Figure S3, Supporting Information). As a comparison to the Fe_2O_3 catalyst, CoO_x and RuO_x were also synthesized analogously and characterized using

TEM and XRD (Figures S4 and S5, Supporting Information). Furthermore, Raman spectroscopy was performed on Fe–N–C and XC72 supports, showing similar graphitic content between the catalyst supports, Figure S6, Supporting Information.

To evaluate the chemical state of the $\text{Fe}_2\text{O}_3/\text{Fe-N-C}$ catalyst and the potential electronic structure changes triggered by interactions between Fe–N_x sites and Fe_2O_3 nanoparticles, atomic resolution electron energy loss spectroscopy (EELS), X-ray absorption spectroscopy (XAS), and XPS were utilized. EELS was used to probe the valence state of the single-atom Fe and the Fe_2O_3 sites. Figure 2a shows the locations where EELS spectra were taken for Fe_2O_3 particles (locations 1 and 2) and single atom Fe sites (locations 3 and 4). Both spectra show the Fe-L_{3,2} edges, however, there is an L₃, L₂ excitation edge shift to lower energy loss and reduced L₃/L₂ white line ratio for single atom Fe (peak spacing of 12.4 eV), compared to Fe_2O_3 (13.2 eV) in Figure 2b. This energy shift and quantitative analysis of the Fe-L₃/L₂ edges suggest the single atom Fe to be in an oxidation state lower than Fe^{3+} , in agreement with our previous work

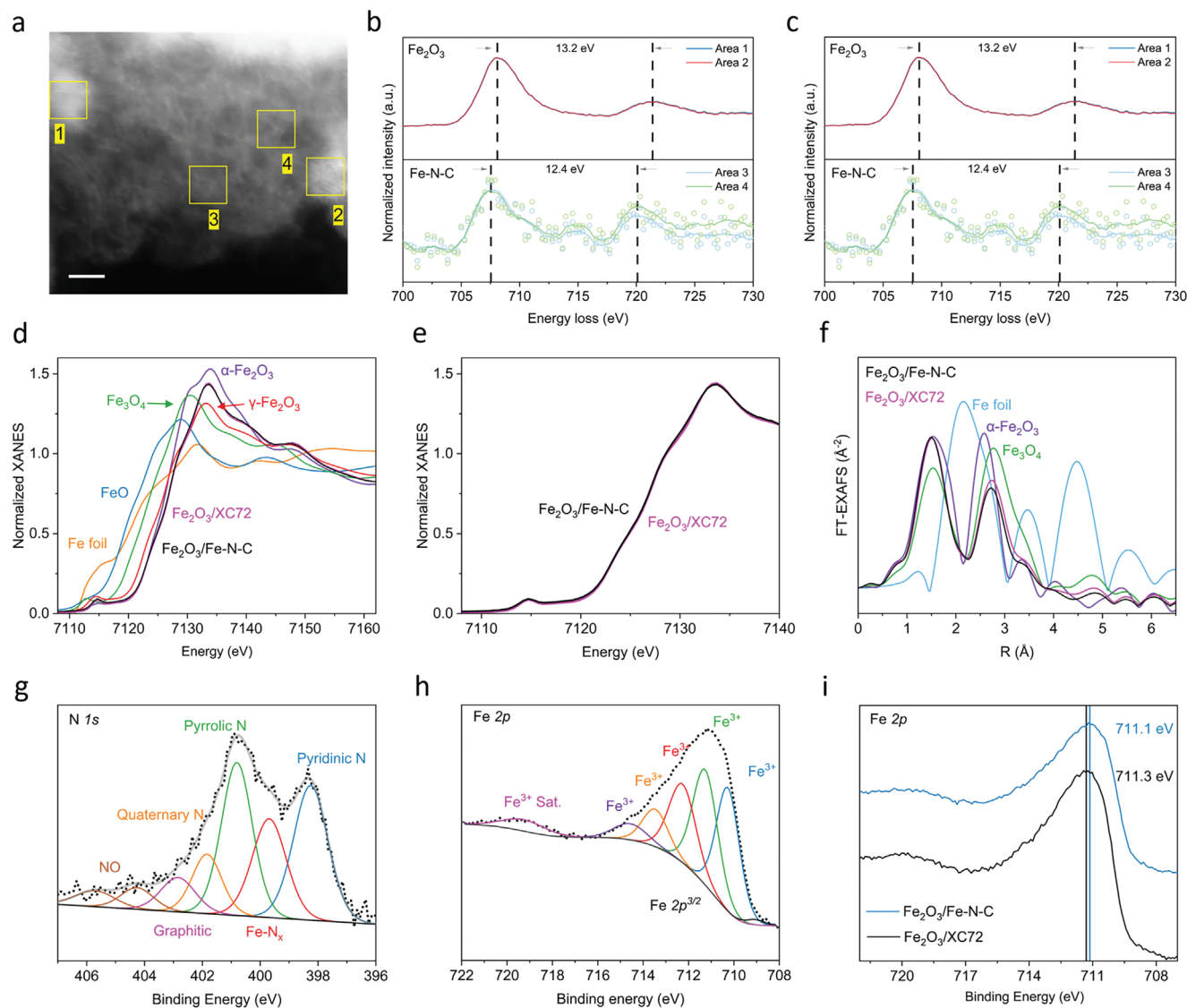


Figure 2. Local chemical and coordination environment of the Fe_2O_3 nanoparticle catalysts. a) AC-STEM image and EELS spectra locations on the $\text{Fe}_2\text{O}_3/\text{Fe-N-C}$ catalysts, scale bar is 2 nm. b) EELS spectra of the $\text{Fe-L}_{3,2}$ edges of the Fe_2O_3 nanoparticle (top) and atomically dispersed Fe-N_x sites (bottom). c) EELS spectra comparing the energy loss of the $\text{Fe-L}_{3,2}$ edge of the Fe_2O_3 supported on Fe-N-C or XC72. Fe K-edge XAS data for the Fe_2O_3 catalysts supported on both Fe-N-C and XC72. d) XANES spectra with the corresponding references and e) XANES spectra comparing Fe_2O_3 supported on XC72 versus Fe-N-C . f) Fourier transformed (k^2 -weighted) EXAFS of the $\text{Fe}_2\text{O}_3/\text{Fe-N-C}$ catalyst and corresponding references. XPS spectra for the $\text{Fe}_2\text{O}_3/\text{Fe-N-C}$ catalyst, h) N 1s spectra, and i) Fe 2p XPS spectra. j) Comparison of the Fe 2p XPS spectra for the Fe_2O_3 catalyst supported on Fe-N-C or XC72.

where Fe-N-C has an oxidation state $\text{Fe}^{2.6+}$.^[28] At the same time, the analysis for the Fe_2O_3 nanoparticles indicated an oxidation state of Fe^{3+} , in agreement with the XAS and XPS (Figure S7, Supporting Information) results. Atomic resolution EELS was further applied for a highly localized evaluation of possible Fe_2O_3 and Fe-N_x interactions modifying the electronic structure of the nanoparticles. Comparing the $\text{Fe-L}_{3,2}$ edges of the Fe_2O_3 nanoparticles supported on Fe-N-C or XC72 reveals a 0.1 eV shift in the energy loss, Figure 2c. Such small shifts in energy loss can arise due to experimental conditions and inaccuracies in the selected method for spectra processing (something that requires extreme care and is system-dependent).^[30] Therefore,

further complementary techniques are employed to evaluate possible nanoparticle–single atom interactions.

XANES of the Fe K-edge (7112 eV) was employed to investigate the chemical state of the Fe_2O_3 nanoparticles on both supports, Figure 2d. The Fe K-edge XANES spectra for both Fe_2O_3 catalysts again confirm that Fe is in a Fe^{3+} oxidation state. The XANES spectra for the catalysts are in between those for the $\gamma\text{-Fe}_2\text{O}_3$ and $\alpha\text{-Fe}_2\text{O}_3$ references. We thus further refer to these γ species simply as Fe_2O_3 . Note that our previous work, utilizing the same Fe-N-C suggests the Fe-N_x sites to be in a $\text{Fe}^{2.6+}$ oxidation state.^[28] Again, to evaluate possible Fe_2O_3 (Fe^{3+}) and Fe-N_x ($\text{Fe}^{2.6+}$) interactions, the rising edge and pre-edge of the Fe_2O_3 supported

on Fe–N–C and XC72 were compared, as shown in Figure 2e, however, no meaningful shifts in the energy were observed. The local coordination of Fe species was further analyzed by Fourier-transform extended X-ray adsorption fine structure (FT-EXAFS) in Figure 2f. For the Fe₂O₃ catalysts, regardless of the support, two dominating peaks are observed. One at a low bond distance (≈ 1.4 Å, phase uncorrected), corresponding to the expected Fe–O coordination and one at a larger bond distance (≈ 2.6 Å, phase uncorrected), which corresponds to the Fe–Fe coordination in Fe₂O₃, and is in agreement with the Fe-oxide reference materials. As shown in our previous work, the EXAFS for the Fe–N–C supports exhibits only one peak at low bond distance for Fe–N, confirming its atomically dispersed nature.^[28] The corresponding EXAFS *k*-space analysis is shown in Figure S8, Supporting Information.

To further investigate the chemical environment and coordination of the Fe species, XPS was performed. Figure 2h shows the N 1s spectra for the Fe₂O₃/Fe–N–C catalyst, confirming the Fe–N_x coordination, along with the (NO₃RR active) pyridinic and pyrrolic N-moieties, characteristic of the Fe–N–C support (XPS for the Fe–N–C support is given in Figure S9, Supporting Information). From the deconvoluted Fe 2p spectra in Figure 2i, the oxidation state of Fe₂O₃ is Fe³⁺, regardless of the support used, further corroborating the EELS and XANES analysis. Full XPS deconvolution of the C 1s, O 1s, N 1s, and Fe 2p spectra for the Fe₂O₃/Fe–N–C and Fe₂O₃/XC72 catalysts are shown in Figures S7 and S10, Supporting Information, respectively. Again, to elucidate possible particle-single atom interactions, the Fe 2p spectra between the Fe₂O₃ supported on Fe–N–C and XC72 were compared, Figure 2j, a binding energy shift of ≈ 0.2 eV is observed, comparable to that of recent nanoparticle-single atom reports in the literature.^[31–33] However, binding energy shifts during the deconvolution and calibration (commonly to features in C 1s spectrum) of the spectra, can easily induce binding energy shifts on the level of 0.2 eV, especially when the complex nature of the carbon is changing in the compared catalyst supports.^[34]

It should be noted that as the popularity of nanoparticle/single atom support systems increases, extreme care must be taken in the interpretation of the chemical state. Often nanoparticle/single atom support electronic interactions are claimed exclusively through ambiguous shifts in the XPS spectra, and subsequently used as the foundation for interesting computational models and reaction mechanisms and attributed to any increased activity and stability. In this work, after rigorously investigating the electronic structure of the Fe₂O₃ supported on atomically dispersed Fe–N–C and XC72 supports, with highly localized, bulk, and surface sensitive techniques (EELS, XAS, and XPS), no spectroscopically detected interactions were observed. Critically, however, this does not rule out the possibility of electronic interactions between the Fe₂O₃ nanoparticles and Fe–N_x sites enhancing NO₃RR performance. These highly sensitive interactions might require probing through electrochemical processes, in which the nanoparticle is active, while the M–N_x site is inert, such that CO stripping experiments for Pt/M–N–C, allowing changes in the onset potentials or peak shapes to reflect interactions between the nanoparticle and M–N_x site. Regardless, a Fe₂O₃/Fe–N–C active particle-active support catalyst has been synthesized and robustly charac-

terized. The Fe₂O₃/Fe–N–C catalyst contains a multitude of highly active NO₃RR sites at both the nanoparticle and single atom scales, which are synergized, enhancing the NO₃RR performance.

2.2. Electrochemical NO₃RR performance

Linear sweep voltammetry (LSV) was performed in an alkaline, 1 M KOH + 0.16 M KNO₃ electrolyte to assess the NO₃RR activity of the blank carbon paper, XC72, and Fe–N–C catalyst supports, and the Fe₂O₃ nanoparticles supported on both XC72 and Fe–N–C, as shown in Figure 3a. From the LSV there is a slight positive shift in the reaction onset potential (-0.59 V vs. RHE) in comparison to the blank carbon paper electrode, when using XC72, indicating that even the metal-free carbon support has some, albeit limited NO₃RR performance. Note in this work all potentials are reported against the reversible hydrogen electrode, RHE. Employing the Fe–N–C catalyst support realizes a significant positive shift in the reaction onset potential (-0.34 V). Interestingly, despite having increased j_{NH_3} at higher overpotentials in alkaline media, the Fe–N–C was observed in our previous work to have a higher selectivity to NH₃ at less cathodic potentials in neutral media (0.05 M PBS), which could be due to its hyperactivity toward reducing the NO₂[−] intermediate in the NO₃RR $2e^- + 6e^-$ transfer pathway, often formed at lower pH, which is suppressed in alkaline media.^[27,28] The addition of Fe₂O₃ nanoparticles further shifts the reaction onset potential even more positively to -0.14 V, regardless of either the XC72 or Fe–N–C support. However, at more cathodic potentials, the current of Fe₂O₃/Fe–N–C dominates due to additional activity provided by the active Fe–N_x sites in the Fe–N–C support. Figure S11, Supporting Information shows the LSV comparison of the Fe, Co, and Ru oxides supported on XC72, where RuO_x shows the most positive onset potential (approximately $+0.05$ V, however, is quickly out-competed by HER). Figures S4 and S5, Supporting Information show the LSV performance of CoO_x and RuO_x in electrolytes with and without KNO₃. To evaluate the catalytic performance of the supports towards the NO₃RR, chronoamperometry measurements were performed at potentials between -0.20 and -1.20 V as shown in Figure 3b. The XC72 support has negligible activity until -0.8 V and reaches a maximum FE_{NH_3} of 55%. However, the Fe–N–C support demonstrates superior activity, holding a FE_{NH_3} of $\approx 80\%$ above -0.20 V, reaching a maximum of 90% at -0.40 V and a maximum $Yield_{\text{NH}_3}$ of $2.9 \text{ mmol}_{\text{NH}_3} \text{ h}^{-1} \text{ cm}^{-2}$ (at an NH₃ partial current density, $j_{\text{NH}_3} = 490 \text{ mA cm}^{-2}$ at -1.20 V), surpassing other reported Fe–N–C catalysts for the NO₃RR (or 135 mA cm^{-2} at -0.6 V).^[12,29] The addition of Fe₂O₃ nanoparticles enhances the FE_{NH_3} (after -0.20 V) and significantly improves the $Yield_{\text{NH}_3}$ over the potential range reaching a maximum of $6 \text{ mmol}_{\text{NH}_3} \text{ h}^{-1} \text{ cm}^{-2}$ ($j_{\text{NH}_3} = 1265 \text{ mA cm}^{-2}$), Figure 3c. Furthermore, Fe₂O₃/Fe–N–C demonstrates increased FE_{NH_3} and $Yield_{\text{NH}_3}$ over the potential range compared to Fe₂O₃/XC72. Interestingly, the Fe₂O₃/Fe–N–C can maintain a FE_{NH_3} of 90–95% over the potential range, highlighting the catalysts' potential independent NH₃ selectivity, resisting the parasitic HER even at highly cathodic potentials.

Having established the superior performance of the Fe₂O₃/Fe–N–C catalyst, a Fe₂O₃ loading study was performed by adjusting

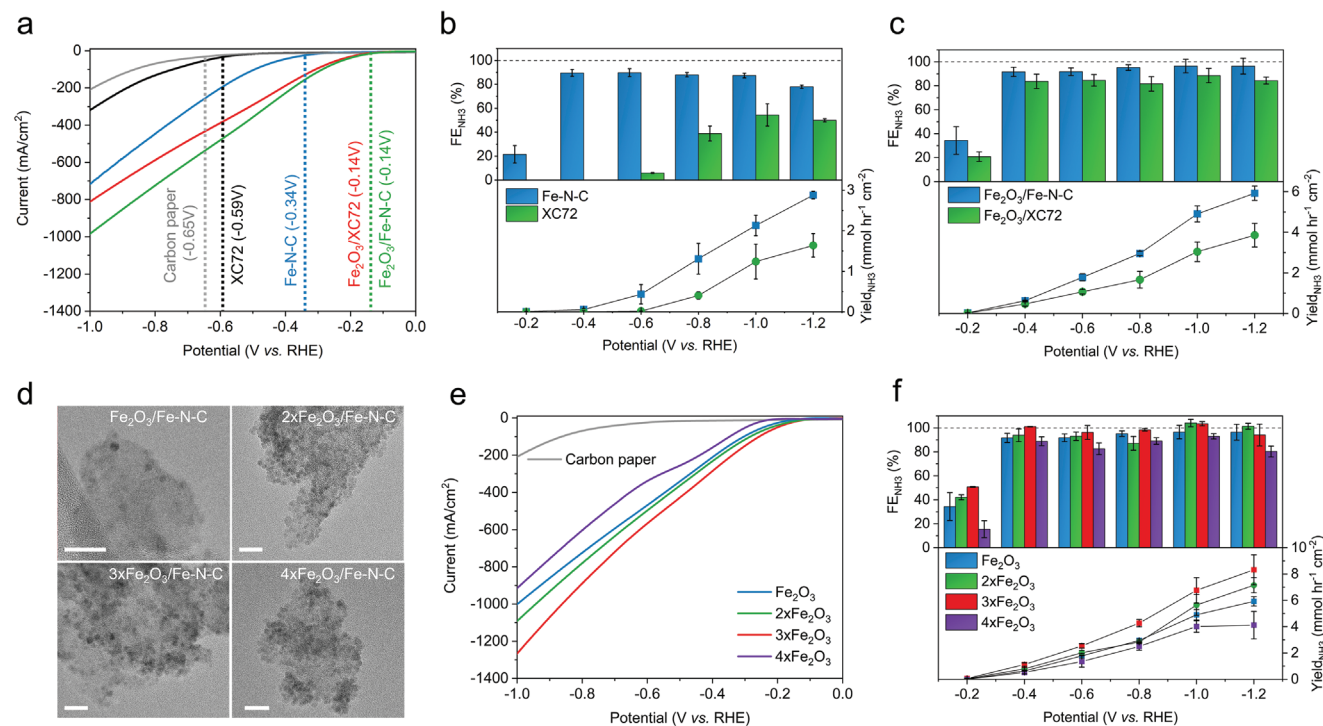


Figure 3. Electrochemical NO_3RR performance of Fe_2O_3 based catalysts and supports in 1 M KOH + 0.16 M KNO_3 electrolyte. a) Linear sweep voltammetry at a scan rate of 5 mV s^{-1} . The red line is $\text{Fe}_2\text{O}_3/\text{XC72}$ and the green line is $\text{Fe}_2\text{O}_3/\text{Fe-N-C}$. Chronoamperometry measurements for 15 min at applied potentials from -0.20 to -1.20 V versus RHE. b) comparing XC72 versus Fe-N-C catalyst supports and c) comparing $\text{Fe}_2\text{O}_3/\text{Fe-N-C}$ versus $\text{Fe}_2\text{O}_3/\text{XC72}$. d) TEM images of increasing Fe_2O_3 loadings supported on Fe-N-C, the scale bar is 20 nm. Electrochemical performance of $\text{Fe}_2\text{O}_3/\text{Fe-N-C}$ with varying Fe_2O_3 loadings, e) Linear sweep voltammetry at a scan rate of 5 mV s^{-1} and f) Chronoamperometry measurements for 15 min at applied potentials from -0.20 to -1.20 V versus RHE with a catalyst loading on the carbon paper of 0.2 mg cm^{-2} . The corresponding chronoamperometry measurements and UV-vis NH_3 quantification are given in Figures S20–S25, Supporting Information. Note that all samples for the NO_3RR performance in this figure have undergone a pre-reduction activation step, the impact of which is discussed in detail later in the manuscript.

the $\text{Fe}(\text{acac})_3$ loading, to further enhance the NO_3RR activity. The TEM images in Figure 3d show the $\text{Fe}(\text{acac})_3$ loading impact on the Fe_2O_3 site density and gradual formation of agglomerates. With the standard Fe_2O_3 (e.g., $1 \times \text{Fe}(\text{acac})_3$), a relatively low Fe_2O_3 site density is observed with no agglomerates. The optimal loading appears to be at $3 \times \text{Fe}_2\text{O}_3$, at this loading, the Fe_2O_3 site density significantly increases, with slight agglomerate formation beginning, while at $4 \times \text{Fe}_2\text{O}_3$, the agglomerated features dominate, reducing the catalytically active surface area. Figures S12–S15, Supporting Information shows additional TEM images for the $\text{Fe}_2\text{O}_3/\text{Fe-N-C}$ at loadings between $1 \times$ – $4 \times \text{Fe}(\text{acac})_3$. Thermogravimetric (TGA) analysis, Figure S16, Supporting Information determined a Fe weight loading of 42% for the $3 \times \text{Fe}_2\text{O}_3$ catalyst and 22% for the $1 \times \text{Fe}_2\text{O}_3$, indicating a non-linear increase in the Fe content with precursor loading. The optimal $3 \times \text{Fe}_2\text{O}_3$ loading is directly observed in the NO_3RR performance and calculated ECSA, Figure 3e and Figure S17, Supporting Information, respectively. Furthermore, $3 \times \text{Fe}_2\text{O}_3/\text{Fe-N-C}$ demonstrates the highest FE_{NH_3} maintaining $\approx 95\text{--}100\%$ from -0.40 to -1.20 V , and the highest $\text{Yield}_{\text{NH}_3}$ at all potentials, reaching a maximum of $8.3 \text{ mmol}_{\text{NH}_3} \text{ h}^{-1} \text{ cm}^{-2}$ ($j_{\text{NH}_3} = 1785 \text{ mA cm}^{-2}$). To further optimize the catalyst performance and increase j_{NH_3} , the optimal catalyst loading on the carbon paper was investigated. The ink volume of $3 \times \text{Fe}_2\text{O}_3/\text{Fe-N-C}$ drop cast on the carbon paper electrode was varied to achieve a final

catalyst loading between $0.2\text{--}10.0 \text{ mg cm}^{-2}$. LSV was performed to screen the activity of the different catalyst loadings, shown in Figure S18, Supporting Information. As the catalyst loading increased from $0.2\text{--}1.0 \text{ mg cm}^{-2}$, the maximum current increased, and the reaction onset potential shifted positively, with no improvement being observed between $0.5\text{--}1.0 \text{ mg cm}^{-2}$. However, after 1.0 mg cm^{-2} the catalyst layer becomes too thick, inhibiting the optimal use of the porous carbon paper, resulting in reduced activity, with 10.0 mg cm^{-2} giving the lowest performance. As an activity comparison, Figure S18c, Supporting Information shows the reaction onset potential and maximum current at -0.5 V (the maximum potential at which a cathodic energy efficiency of 30% is achieved assuming 100% FE_{NH_3}). The optimal catalyst loading is determined to be 0.5 mg cm^{-2} , giving an onset potential of approximately -0.13 V and a current density of 520 mA cm^{-2} at -0.50 V . Therefore, the optimal catalyst is the $3 \times \text{Fe}_2\text{O}_3/\text{Fe-N-C}$ with a loading of 0.5 mg cm^{-2} , and the electrochemical results discussed further in this manuscript utilize these conditions. Finally, to confirm that the source of NH_3 originates from the NO_3^- in the electrolyte, rather than contamination or decomposition of the N-doped carbon support, a series of control experiments were performed. Electrolysis from -0.2 to -1.2 V for 15 min each was performed in 1 M KOH electrolyte (without NO_3^-) and tested by UV-vis, showing no detected NH_3 in the absence of NO_3^- , Figure S19a,b, Supporting Information. Next, isotopically

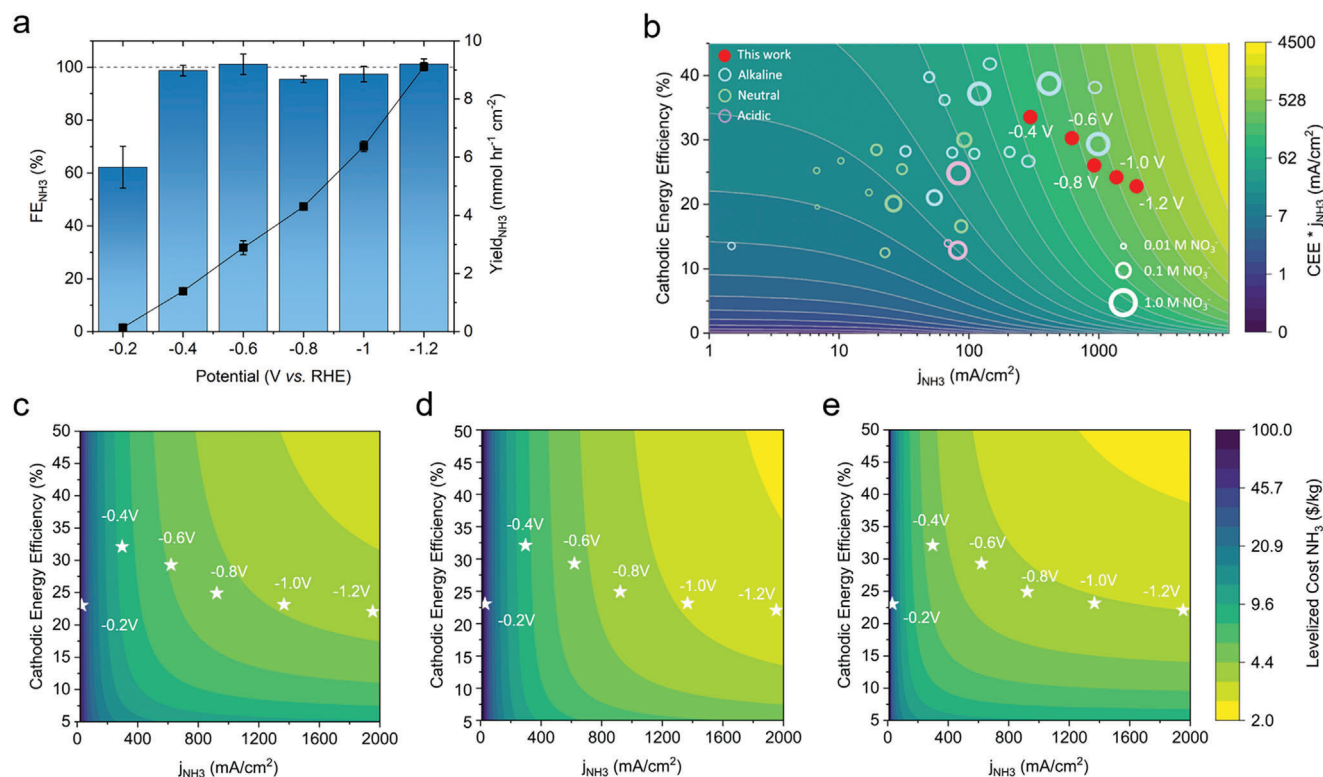


Figure 4. Electrochemical NO_3RR performance of the optimized $3\times\text{Fe}_2\text{O}_3/\text{Fe-N-C}$ catalyst with a 0.5 mg cm^{-2} catalyst loading on the carbon paper electrode in a $1\text{ M KOH} + 0.16\text{ M KNO}_3$ electrolyte. a) Optimized FE_{NH_3} and $Yield_{\text{NH}_3}$ as a function of applied potential. b) Comparison of NO_3RR performance in the current literature, evaluating the cathodic energy efficiency versus j_{NH_3} . Full details and references for each reported NO_3RR system are provided in Table S1, Supporting Information. Contour plots evaluating the trade-off of cathodic energy efficiency versus j_{NH_3} on the levelized cost of NH_3 for cases with c) grid electricity price, d) idealized cost of renewable energy, and e) reduced electrolyzer stack cost. Where performance improves across contours towards the top right corner.

labeled experiments were performed using a $1\text{ M KOH} + 0.16\text{ M }^{15}\text{KNO}_3$ electrolyte. Electrolysis was performed at -1.0 V for 15 min , and $^1\text{H NMR}$ quantified the $^{15}\text{NH}_3$ produced. The isotopic measurements (Figure S19c,d, Supporting Information) show a strong comparison between the non-isotopically doped experiments, both at a $FE_{\text{NH}_3} \approx 100\%$ and a yield rate of $6.5\text{ mmol h}^{-1}\text{ cm}^{-2}$ ($^{15}\text{KNO}_3$) and $6.2\text{ mmol h}^{-1}\text{ cm}^{-2}$ ($^{14}\text{KNO}_3$), confirming that any NH_3 detected results from the activation of NO_3^- .

Figure 4a, shows the NO_3RR performance of the optimized $3\times\text{Fe}_2\text{O}_3/\text{Fe-N-C}$ catalyst (with a 0.5 mg cm^{-2} loading on the working electrode), maintaining a FE_{NH_3} above 95% over the entire -0.40 to -1.20 V potential range, again highlighting its potential independent nature towards NH_3 selectivity. This potential independent behavior on NH_3 selectivity provides an advantage in practical systems. When coupled with renewable energy, dynamic changes in the supplied energy can lead to cell voltage fluctuations. With the current system, even with cell voltage fluctuations, the product purity would remain unchanged. A maximum $Yield_{\text{NH}_3}$ of $9.2\text{ mmol h}^{-1}\text{ cm}^{-2}$ is achieved ($j_{\text{NH}_3} = 1950\text{ mA cm}^{-2}$) at $\approx 100\% FE_{\text{NH}_3}$. To compare the performance of the $3\times\text{Fe}_2\text{O}_3/\text{Fe-N-C}$ catalyst to the current NO_3RR literature, Figure 4b compares the cathodic energy efficiency, CEE (assuming the thermodynamic reduction potential for the anodic oxygen evolution reaction) versus the j_{NH_3} . The CEE is a function of the FE_{NH_3} and applied potential (taking a penalty for highly ca-

thodic potentials), while the j_{NH_3} is a function of the FE_{NH_3} and total current, enabling a comparison beyond just the FE_{NH_3} or $Yield_{\text{NH}_3}$, which can vary significantly based on the applied potential. Larger circles indicate higher concentrations of NO_3^- , often resulting in better performance, while colors are used to designate acidic, neutral, or alkaline media. The contours in Figure 4b are the product of $(CEE \times j_{\text{NH}_3})$, yielding a performance metric in terms of mA cm^{-2} , which is optimized across contours and towards the top right. From Figure 4b, it is apparent that universally, the NO_3RR suffers from relatively low energy efficiencies at meaningful j_{NH_3} (above 100 mA cm^{-2}), due to the thermodynamic reaction onset potential (0.69 V vs RHE , $\text{pH} = 14$), while more cathodic potentials (approximately -0.40 to -0.80 V) are typically required to achieve large j_{NH_3} . The majority of the NO_3RR performances in the literature report limited j_{NH_3} , less than 100 mA cm^{-2} , or utilize expensive PGM metals to realize higher j_{NH_3} , hindering industrial relevance. The $3\times\text{Fe}_2\text{O}_3/\text{Fe-N-C}$ catalyst (red circles) enables high current densities even at mildly reductive potentials, 297 mA cm^{-2} with a cathodic energy efficiency of 33% . The potential independent nature of the NH_3 selectivity, allows the $3\times\text{Fe}_2\text{O}_3/\text{Fe-N-C}$ system to be operated between -0.40 to -1.20 V at nearly $100\% FE_{\text{NH}_3}$, giving ultra-high j_{NH_3} from 297 to 1950 mA cm^{-2} , outperforming the current NO_3RR literature (see Figure S26, Supporting Information for a linear j_{NH_3} scale).

There is significant ambiguity in determining the optimal cathodic potential to yield both, an acceptable CEE and j_{NH_3} and depends on many factors including catalyst cost, device costs, CAPEX and OPEX costs, the levelized cost of NH_3 as j_{NH_3} increases, and many others. To offer a semi-quantitative optimal trade-off between energy efficiency and j_{NH_3} , Figure 4c–e offers a simplified economic analysis inspired by a recent work from Daiyan et al.^[22] To construct meaningful contours, the levelized cost of NH_3 ($\text{\$ kg}^{-1}$) was determined as a function of the CAPEX, OPEX, and yield rates of NH_3 . These inputs consider the increasing OPEX as the cathodic potential increases, therefore decreasing energy efficiency, while also accounting for increased production rates of NH_3 (see Experimental Section for details). Three scenarios are considered, where the electricity cost varies from standard grid electricity at $\text{\$0.07 kWh}^{-1}$ (Figure 4c), idealized renewable energy from solar power at $\text{\$0.03 kWh}^{-1}$ (Figure 4d), and with a decreased CAPEX resulting from reduced electrolyzer stack costs (Figure 4e). From these contour plots, it is readily observed that the most effective way to cross contours (until $\approx 1 \text{ A cm}^{-2}$) is through increasing the j_{NH_3} , rather than achieving low j_{NH_3} with increasing energy efficiency. This is observed for both electricity price scenarios, the lowest levelized cost of NH_3 is achieved at the most cathodic potential of -1.2 V , where the ultrahigh current density (j_{NH_3} of -1.95 A cm^{-2}) is achieved, despite the lower energy efficiency. Interestingly, the impact of energy efficiency has a minor effect at small/moderate j_{NH_3} and becomes more effective at higher j_{NH_3} .

2.3. In Situ Evaluation of Fe Speciation during Pre-Reduction Activation and Electrolysis

Prior to the NO_3RR measurements, a pre-reduction activation step was performed and found to significantly improve the activity of the catalyst, as demonstrated through the LSV in Figure 5a. The pre-reduction activation applies a highly reductive potential of -1.5 V versus RHE for 90 s. To elucidate the chemical state changes of the pristine $3\times\text{Fe}_2\text{O}_3/\text{Fe-N-C}$ to the now highly active catalyst, in situ quick XAFS was performed and complemented by post-mortem XPS. Note that a milder electrolyte of $0.1 \text{ M KOH} + 0.016 \text{ M KNO}_3$ was used for the in situ experiments in order to preserve the integrity of the Kapon used in the operando spectroscopy cell. Figure 5b,c show the XANES spectra of the Fe K-edge under NO_3RR conditions for the $3\times\text{Fe}_2\text{O}_3/\text{Fe-N-C}$ catalyst, without and with the pre-reduction activation step, respectively. Prior to any electrochemical measurements, an initial spectrum was taken at OCV, indicated by the gray curve. Figure S27, Supporting Information demonstrates that there are no significant changes between the air measurements and OCV samples, indicating no changes in the Fe chemical state prior to the applied potential. In Figure 5b, for the sample without the activation step, a potential of -1.0 V was directly applied, and Fe K-edge XAS spectra were recorded every 3 s (with every two spectra being averaged for increased quality), for the first 90 s. Immediately, there is a distinct shift in the absorption edge toward lower energy, with a simultaneous decrease in the pre-edge feature $\approx 7114 \text{ eV}$ and a significant increase in the intensity of the white line. A final spectrum was acquired after 15 min of a potential hold at -1.0 V (analogous to the NO_3RR experiments dis-

cussed earlier), which demonstrates that changes in the Fe chemical state after the initial 90 s are relatively minor. By comparing these spectra with the Fe-reference materials, it is concluded that in the absence of a pre-reduction activation step, the NO_3RR conditions induce a transformation of Fe^{3+} to Fe^{2+} . In particular, the final in situ spectrum resembles strongly the $\text{Fe}(\text{OH})_2$ spectrum.^[35] In contrast, Figure 5c shows the evolution of Fe K-edge XAS for the catalyst, where the 90 s pre-reduction activation step at -1.5 V has been performed. In this scenario, the changes in Fe K-edge XANES during the first 90 s are remarkably different. The white line intensity decrease is accompanied by a shift in the edge position towards lower energy and an increase in the pre-edge feature $\approx 7114 \text{ eV}$. After the 90 s of activation, a -1.0 V potential was applied (replicating the NO_3RR tests, in which an initial 90-s activation at -1.5 V is followed by -1.0 V for 15 min). The XAS spectra collected during this latter stage show a further reduction in the white line intensity and an increase in the pre-edge feature, likely associated with the further reduction of Fe^{3+} (or intermediate Fe^{2+}) and the formation of metallic Fe (Fe^0). These results show clearly that the evolution of the chemical state of the Fe is very different in cases with and without the activation step (Figure S28, Supporting Information).

To quantitatively analyze the Fe speciation observed in the in situ quick XAFS experiments, principal component analysis (PCA) and multivariate curve resolution (MCR) are employed and complemented by the EXAFS fitting.^[36–39] PCA and MCR methods were applied to a combined dataset, consisting of spectra collected in the experiment with and without the activation step. First, PCA identified three spectroscopically distinct species in this combined dataset, as determined by a Scree plot (Figure S29, Supporting Information), showing the relative importance of the principal components. Next, MCR analysis based on the alternating least squares (MCR-ALS) method was used to determine the spectra corresponding to these three species, and the corresponding concentration profiles. For this purpose, a MATLAB code developed by Jaumont et al. was employed.^[40] A successful convergence was achieved after eight iterations. The details of the fits are shown in Table S2, Supporting Information and discussed in Note S1, Supporting Information. The three spectral components identified by the MCR-ALS method are shown in Figure S30, Supporting Information. Spectral component 1 aligns well with the spectrum of metallic Fe in the Fe^0 state. Spectral component 2 resembles the spectrum for $\text{Fe}(\text{OH})_2$, and thus, can be associated with the Fe^{2+} state. Finally, spectral component 3 matches well with the $3\times\text{Fe}_2\text{O}_3/\text{Fe-N-C}$ sample and the spectrum of metallic Fe in the Fe^0 state. Figure 5d shows the evolution of the concentration of these identified Fe species over the 15 min NO_3RR electrolysis at -1.0 V , for the $3\times\text{Fe}_2\text{O}_3/\text{Fe-N-C}$ without the pre-reduction activation. Figure 5d shows that immediately after the -1.0 V is applied, nearly all the Fe^{3+} is converted to Fe^{2+} , likely in the form of $\text{Fe}(\text{OH})_2$. In the following 15 min of the experiment, some Fe^{2+} is further reduced to Fe^0 , but at a very slow rate. In contrast, Figure 5e shows the concentration profiles of Fe species obtained for the case with a pre-reduction activation step. During the first 25 s of the 90 s potential hold at -1.5 V , the conversion from Fe^{3+} to Fe^{2+} is paralleled by the formation of metallic Fe^0 . During the 15 min electrolysis at -1.0 V , the remaining Fe^{2+} is further converted to Fe^0 until H550 s, at which point the concentration of Fe^{3+} , Fe^{2+} ,

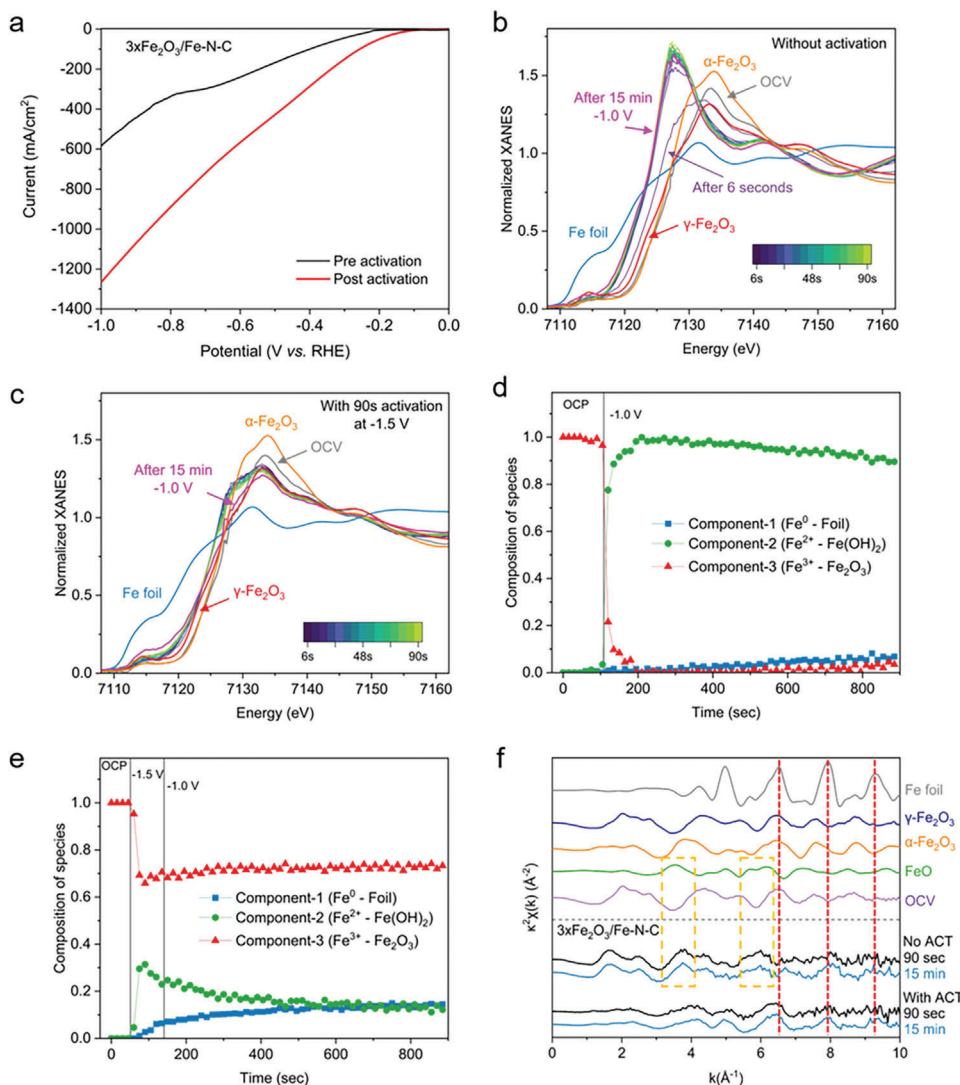


Figure 5. In situ investigation of the electronic state of Fe during the pre-reduction activation step and NO_3RR electrolysis of the $3\times\text{Fe}_2\text{O}_3/\text{Fe-N-C}$. a) LSV in 1 M KOH + 0.16 M KNO_3 demonstrating the increased activity from the pre-reduction activation step. b) XANES spectra of the catalyst in the first 90 s of the NO_3RR at -1.0 V and after 15 min, for the catalyst b) without the pre-reduction activation step and c) with the pre-reduction activation step. Fe speciation over 15 min of NO_3RR electrolysis at -1.0 V as determined from MCR-ALS analysis of the in situ XANES measurements for the catalyst d) without the pre-reduction activation step and e) with the pre-reduction activation step. f) EXAFS spectra in k -space analysis of the in situ measurements, where the EXAFS features related to Fe oxide structures are marked by orange dashed rectangles and features related to metallic Fe are marked by red dashed lines.

and Fe^0 approaches the steady state. Thus, at the highly cathodic potential of -1.5 V, the reduction of Fe^{3+} to Fe^0 is triggered, at which point the further reduction of Fe^{3+} is hindered. These results agree well with previously reported literature demonstrating that during a cathodic bias of -1.0 V, Fe oxides supported on nitrogen-doped carbon were not fully reduced to Fe^0 , which was attributed to phase contractions and the insertion of H_2O in the lattice, maintaining a $\text{Fe}(\text{OH})_2$ structure (Fe^{2+}), despite being 560 mV lower than thermodynamically expected potential for Fe^0 .^[41] Additionally, it has been shown that nitrogen dopants can stabilize Fe^{2+} species, preventing the complete reduction to Fe^0 under a cathodic bias.^[42] The in situ EXAFS data in k -space shown in Figure 5f agrees with the XANES analysis, showing the

clear formation of Fe^0 during the pre-reduction activation step and further formation during the 15 min electrolysis, resembling the Fe foil reference. For the sample without the activation step, during the electrolysis, the characteristic Fe^0 high-frequency oscillations at larger k -values are also present, however, they are much less pronounced than in the case with the pre-reduction activation step. Further analysis of the EXAFS spectra in Figure S31, Supporting Information shows that in the experiments with and without the activation step, a Fe–Fe bond contribution is observed after 15 min of applied potential. However, for the sample with the pre-reduction activation, the Fe–Fe coordination numbers are significantly larger (6.2 ± 0.5 vs 1.2 ± 0.5), and the Fe–O bond distances are shorter (1.97 vs 2.12 Å), suggesting a

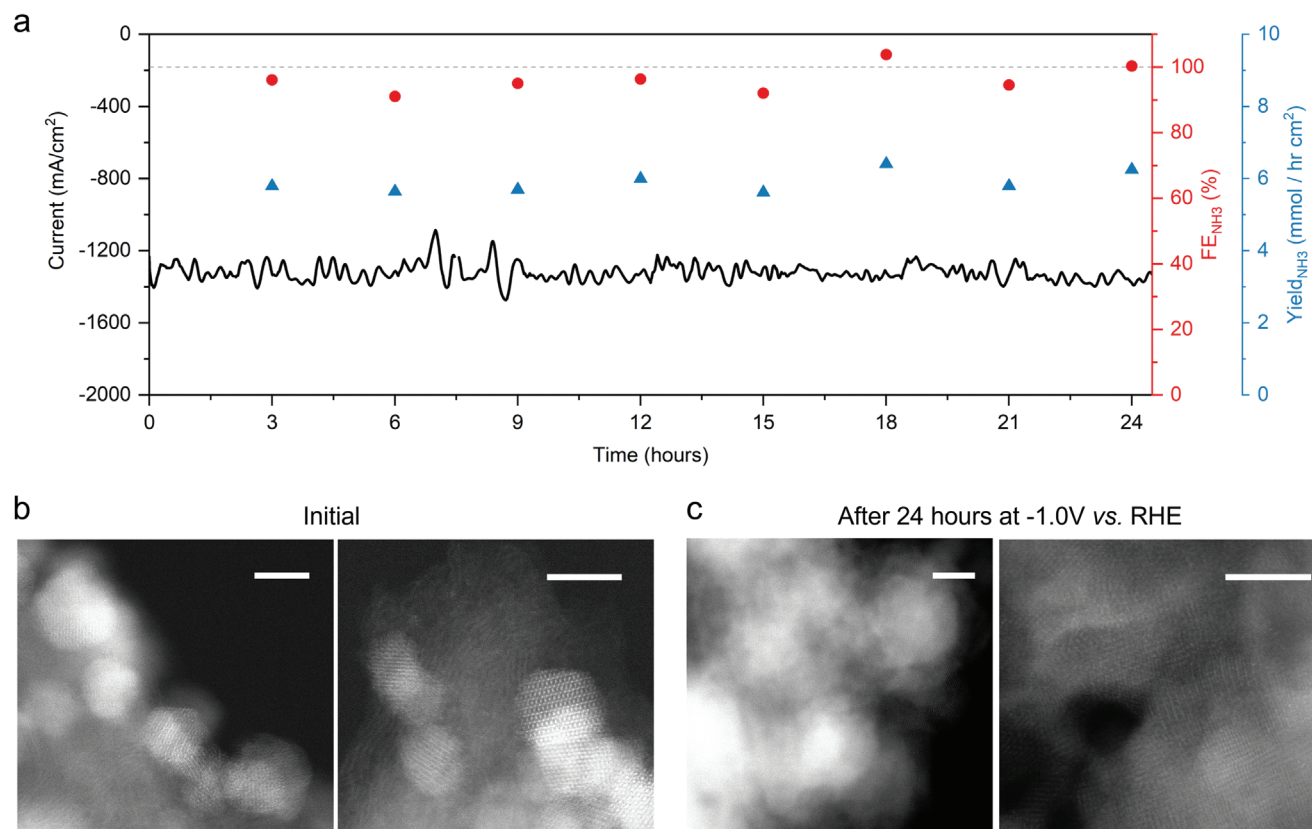


Figure 6. Durability study of the $3\times\text{Fe}_2\text{O}_3/\text{Fe-N-C}$ catalyst. a) 24-h electrolysis at -1.0 V in 1 M KOH + 0.16 M KNO_3 electrolyte. HAADF-STEM images investigating the stability of the Fe_2O_3 nanoparticles b) for the pristine catalyst and c) after the 24-h electrolysis. All scale bars are 5 nm.

larger fraction of Fe^{3+} (e.g., $\gamma\text{-Fe}_2\text{O}_3$ – 1.97 Å) as compared to Fe^{2+} (e.g., FeOOH – 2.08 Å). Thus, EXAFS data analysis further confirms the conclusions from the XANES analysis that the activated catalyst contains a significant amount of Fe^{3+} species coexisting with Fe^0 , while in the non-activated catalyst mainly Fe^{2+} species exist with significantly smaller amounts of Fe^0 (EXAFS fitting parameters given in Tables S3–S5, Supporting Information).

Our XAS analysis shows that even at the highly cathodic potential of -1.5 V, the complete reduction of Fe^{3+} to Fe^0 is not observed, with a significant portion of Fe^{3+} appearing to be stabilized with the formation of $\text{Fe}^0/\text{Fe}^{2+}$. Furthermore, the formation and preservation of the Fe^0 species correspond to a significantly enhanced NO_3RR performance, which is in agreement with previous works demonstrating the effectiveness of lower oxidation state Fe species towards the NO_3RR .^[43,44] The maintained Fe speciation and boosted activity are supported by a 24 h NO_3RR electrolysis at -1.0 V, following a pre-reduction activation step. To circumvent ultrahigh NH_3 concentrations in the electrolyte and subsequent loss of NH_3 in the gas phase, the electrolysis was performed in eight 3-h segments. Furthermore, the system was modified such that peristaltic pumps were connected to an external reservoir to the working chamber, enabling a working electrolyte volume of 250 mL, with constant circulation. After a 3-h segment, the electrolyte was sampled and refreshed. **Figure 6a** shows a stable current density of approximately -1.3 A cm^{-2} at a FE_{NH_3} between 90–100% and $Yield_{\text{NH}_3}$ of ≈ 6 mmol h^{-1} cm^{-2} . The

stable performance over 24 h suggests that no further changes in Fe speciation are occurring, altering catalyst activity or selectivity to NH_3 . Further highlighting the ability of the $3\times\text{Fe}_2\text{O}_3/\text{Fe-N-C}$ catalyst to preserve this ultrahigh NO_3RR performance at a near 100% FE_{NH_3} , resisting the HER even at highly reductive potentials.

To complement the in situ quick XAFS measurements, post-mortem XPS analysis was performed on the working electrode following the pre-reduction activation step and after the 24-h electrolysis at -1.0 V. Following the pre-reduction activation step and 24-h electrolysis, the working electrode was dried under N_2 and stored in a gas-tight vial pre-purged with N_2 for immediate transport to the XPS. To address possible slight re-oxidation of the surface Fe during the transport of the electrode to the XPS, spectra were taken followed by quick (60 s) Ar^+ ion surface etch and re-sampled (see Note S2, Supporting Information for details, considerations, and oxidation consequences of the Ar^+ etching). Although not as rigorous as in situ quick XAFS, the deconvoluted post-mortem XPS spectra in Figures S32–S34, Supporting Information, although more surface sensitive, show a clear qualitative agreement with the XANES measurements, showing the formation of Fe^{2+} , $\text{Fe}(\text{OH})_2$ and Fe^0 during the pre-reduction activation step. Throughout the 24-h electrolysis, post-mortem XPS shows only a slight further reduction of Fe^{3+} , in agreement with the in situ quick XAFS (first 15 min) and increased formation of Fe^0 . Following the 24-h electrolysis, to investigate changes in the Fe_2O_3 nanoparticle structure and atomically dispersed Fe

sites, atomic resolution STEM was performed, Figure 6b,c (and Figure S35, Supporting Information). A slight coarsening in the Fe₂O₃ nanoparticles is observed (≈ 10 nm), however, the minor physical change in the catalyst structure does not negatively alter the NO₃RR performance as observed in Figure 6c. Additionally, at higher magnification, the coexistence of Fe₂O₃ nanoparticles and atomically dispersed Fe sites are maintained (larger images shown in Figure S36, Supporting Information), confirming the durability of both the active Fe₂O₃ nanoparticle catalyst and active Fe–N–C support at highly reductive potentials. As a comparison, a 24-h stability test at -1.0 V was performed on the Fe₂O₃/XC72 catalyst, shown in Figure S37, Supporting Information. Without the Fe–N_x sites, the stability of the Fe₂O₃ particles is reduced, leading to the formation of large agglomerated structures (rather than slightly coarsened particles as in the case of Fe₂O₃/Fe–N–C). For better visualization of the atomically dispersed sites, a Fe–N–C catalyst without Fe₂O₃ nanoparticles after electrolysis (24 h at -1.0 V) was imaged in Figure S38, Supporting Information. These results are supported by other studies in the literature showing high stability of the Fe–N–C sites under reductive potentials.^[12,29,45] Although it is critical to note that these are ex situ measurements with the sample being exposed to air prior to imaging, which can in some cases enable the re-dispersion of single atoms agglomerated during electrolysis back to their atomically dispersed state.

From the chemical state analysis, it is hypothesized that during the pre-reduction activation step, surface Fe³⁺ species are reduced to highly active Fe⁰, which is preserved throughout the NO₃RR electrolysis maintaining the high NO₃RR activity and selectivity to NH₃ (Figure 6a). Based on this analysis, Fe³⁺/Fe²⁺ sites while active for the NO₃RR are less active than Fe⁰ sites. Therefore, to maximize the NO₃RR performance, a pre-reduction step to reduce Fe³⁺ sites to Fe⁰ is essential to obtain enhanced NO₃RR performance.

2.4. Conclusion

In summary, we have leveraged the high activity of Fe-based catalysts, both at the nanoparticle and single atom level, towards the selective conversion of NO₃⁻ to NH₃. We synergized both, the nano and atomic scales to synthesize an active particle-active support catalyst system, Fe₂O₃/Fe–N–C. The atomically dispersed Fe–N_x sites of the active Fe–N–C support, mixed γ/α Fe-phase, and spinel structure of the Fe₂O₃ nanoparticles were robustly confirmed employing atomic resolution STEM and EELS, XAS, and XPS. The optimized 3 \times Fe₂O₃/Fe–N–C catalyst demonstrated potential independent NO₃RR activity, even at highly reductive potentials, reaching a high $Yield_{NH_3}$ of over 9 mmol h⁻¹ cm⁻² at a FE_{NH_3} of 100%, and a j_{NH_3} up to 1.95 A cm⁻² (at -1.2 V vs RHE). In situ XANES and post-mortem XPS revealed the partial reduction of Fe³⁺ surface sites to highly active Fe⁰ during the pre-reduction activation, which is maintained throughout the NO₃RR electrolysis and is critical in boosting the NO₃RR performance. A durability study at -1.0 V over 24 h demonstrated the robustness of the 3 \times Fe₂O₃/Fe–N–C catalyst, preserving the highly active Fe⁰ sites, maintaining a current of 1.3 A cm⁻² and a FE_{NH_3} of 91–100%. This work introduces a novel active particle-active support catalyst system for the NO₃RR, utilizing a plurality of active sites

at both the nanoparticle and single atom scale, to significantly enhance NO₃RR activity. While elucidating the importance of a pre-reduction activation step to create highly active surface Fe⁰ species, capable of realizing NO₃⁻ reduction to NH₃ at industrially relevant current densities (1.95 A cm⁻²) and near unity FE_{NH_3} .

3. Experimental Section

Synthesis of Fe₂O₃, Co₃O₄, and RuO₂ Supported on XC72: The Fe, Co, and Ru nanoparticle catalysts were synthesized using an organic solvent synthesis, employing an oleic acid and oleylamine ligand pair, commonly employed in nanoparticle synthesis to control the size and dispersion of the nanoparticles. Taking Fe₂O₃ as an example, first 44.8 mg of XC72 carbon and 0.2 mmol of Fe(acac)₂ were dispersed by sonication for 30 min in 40 mL of benzyl ether. Next, the mixture was deaerated by purging N₂ for 30 min. The mixture was then heated to 100 °C and then 400 μ L of oleylamine and 200 μ L of oleic acid were added and the temperature was held for 10 min. Next, the mixture was heated to 180 °C and 1 mL of lithium triethylborohydride was added and the temperature was held for 10 min. The catalyst mixture was then heated to 210 °C and held for 45 min. The catalyst mixture was then centrifuged with ethanol three times before filtration with ethanol, followed by drying at 45 °C in an oven.

The Co and Ru-based particle syntheses were identical, with the 0.2 mmol of Co(acac)₂ and Ru(acac)₂ being added in place of Fe(acac)₂.

Synthesis of Fe–N–C: The atomically dispersed Fe–N–C active support was synthesized using the sacrificial support method (SSM). First, a catalyst mixture of 6.25 g of nicarbazin, 1.25 g of OX-50 (Evonik), 1.25 g of LM150 (Cabot), 0.5 g of stöber spheres (made in-house), and 0.6 g of iron (III) nitrate was added and dispersed by sonication for 30 min in water. The catalyst slurry was then dried for 24 h at 45 °C under continuous stirring. The partially dried slurry was then transferred to an oven for 24 h for complete drying at 45 °C. The catalyst mixture was then ball-milled at 45 Hz for 60 min. Next, the milled catalyst powder underwent pyrolysis in a 5% H₂ / 95% Ar atmosphere for 45 min at 975 °C. The pyrolyzed catalyst was then ball-milled a second time at 45 Hz for 1 h before being etched in a concentrated HF (18 M) solution for 96 h to remove the silica support and any nanoparticles. The etched catalyst was then washed with DI water and filtered until neutral pH before drying. A second pyrolysis under a 10% NH₃ / 90% N₂ atmosphere was performed at 950 °C for 30 min. The catalyst was then ball-milled a third time at 45 Hz for 1 h.

Synthesis of Fe₂O₃/Fe–N–C: The Fe₂O₃ nanoparticles supported on atomically dispersed Fe–N–C (Fe₂O₃/Fe–N–C) were synthesized analogously to the nanoparticle catalyst supported on XC72, with the carbon support being switched for the active Fe–N–C support.

Physical Characterization: Transmission electron microscopy (TEM) was performed on a JEOL JEM-2100F. To obtain atomic resolution images, aberration-corrected scanning transmission electron microscopy (AC-STEM) and energy dispersive X-ray spectroscopy (EDX) were performed on a JEOL ARM300CF (at 300 keV accelerating voltage). The valence state of the γ -Fe₂O₃ nanoparticles and atomically dispersed Fe sites were examined through atomic resolution electron energy loss spectroscopy (EELS) on a Nion UltraSTEM200 microscope equipped with a cold FEG, a C3/C5 aberration correction, and a high-energy resolution monochromated EELS system (HERMES). To suppress beam damage, a lower accelerating voltage of 60 keV was used to collect the EELS spectra. For the spectra acquisition, the energy dispersion was set as 0.29 eV per channel at an exposure time of 500 ms per pixel. Background subtraction in the spectrum was achieved by a power-law function and the de-noising of the spectra was performed by the multivariate weighted principal component analysis (PCA) routine in the Digital Micrograph software. The smoothing of the spectra was achieved by a Savitzky-Golay method with points of window of 15 using the Origin software. For energy loss near edge structure (ELNES) analysis on Fe valence state, the spectra collected from different Fe SA locations were summed up and then averaged to improve the signal-to-noise ratio.

The surface valence and chemical bonds of the catalysts were analyzed by XPS performed using a Kratos AXIS Supra spectrometer with a monochromatic Al K α source (1486.6 eV). A pass energy of 160 eV from 1400 to 5 eV at a step size of 1 eV was used to obtain the survey spectra. No charge neutralization was employed. CasaXPS software was used to analyze the XPS data with the spectrum being calibrated by C 1s sp² peak at (284.8 eV). For analyzing the data, two backgrounds were used, with a linear background being employed for the C 1s and N 1s spectrum, while a Shirley background was used for the N 1s and Fe 2p spectrum. For analysis of the sp² carbon, an asymmetric 50% Gaussian / 50% Lorentzian was applied. While for all other data, a 70% Gaussian / 30% Lorentzian was applied. For the Ar⁺ ion etching experiments, a survey was first taken, followed by an etch and another survey, and continued in fashion. Ar⁺ ions with an energy of 5 keV were used to etch a 2 × 1 mm area for 60 s per etch cycle.

To examine the crystal phase of the catalysts, X-ray diffraction (XRD) patterns were obtained using a Rigaku Ultima-III powder X-ray diffractometer. The iron metal content of the catalysts was quantified by thermogravimetric analysis (TGA) performed on a Netzsch TG 209 F1 Libra. To quantify the graphitic and amorphous content in the two catalyst supports (XC72 and Fe–N–C), Raman spectra were taken on an InVia, Renishaw Corp., UK system.

The ex situ XAS measurements for the Fe₂O₃/Fe–N–C and Fe₂O₃/XC72 catalysts were performed on the SAMBA beamline at the SOLEIL Synchrotron Radiation Facility, Paris, France. The sample was measured in fluorescence mode and references in transmission mode using a Si (220) monochromator for the energy selection. Ionization chambers to measure the X-ray intensity before and after the sample were filled with a mixture of Ar/N₂ (10) or pure Ar (11/12).

In Situ Quick XAFS Measurements: The in situ quick XAFS measurements were carried out at the P64 beamline of the DESY Synchrotron Radiation Facility, Hamburg, Germany. A tapered undulator was used as an X-ray source. A Si (111) channel-cut single-crystal monochromator was used with an oscillation frequency of 0.17 Hz. The intensity of incident X-ray radiation was measured by an ionization chamber filled with pure N₂. The beam size was 0.5 × 0.5 mm². The reference and sample were measured in fluorescence mode using a PIPS detector. For the energy calibration, a γ -Fe₂O₃ reference pellet was measured before each sample measurement for 20 s and then moved out of the beam while the sample was moved into the beam. The in situ measurements were performed in a home-built electrochemical single-compartment cell. The electrolyte used was 0.1 M KOH with 0.016 M KNO₃, which is 10× diluted from the 1 M KOH + 0.16 M KNO₃ used for standard electrochemical experiments. The electrolyte was diluted to remain compatible with the Kapton window of the in situ electrochemical cell. A Biologic SP300 potentiostat was used to control the potential. Two sets of measurements were performed. In the first experiment, the sample was reduced at –1.5 V versus RHE (–2.45 V vs Ag/AgCl) for 90 s as an activation step and then a potential of –1.0 V versus RHE (–1.95 V vs Ag/AgCl) was applied and held for 15 min. In the second experiment, the potential of –1.0 V versus RHE was applied directly without the activation step.

Preparation of the Working Electrode: A carbon paper electrode (AvCarb MGL 370, Fuel Cell Store) was used as the working electrode and was cut to a geometric surface area of 0.25 cm² (0.5 × 0.5 cm). An oxygen plasma and acid treatment (0.5 M H₂SO₄) were employed to remove the PTFE layer on the electrode and increase the hydrophilicity. A catalyst ink comprised of 5 mg of catalyst, 680 μ L of isopropanol, 300 μ L of MilliQ water, and 20 μ L of a 5 wt% Nafion (probe sonicated for 1 min, followed by 30 min in a sonication bath) was drop cast on the electrode. Catalyst loading on the electrode was optimized during the study, by varying the amount of catalyst ink drop cast.

Electrochemical Nitrate Reduction: Electrochemical tests were performed in a customized glass H-cell (Adams & Chittenden), separated by a Celgard 3401 membrane (used as received). A carbon paper with catalyst, a reversible hydrogen electrode (Gaskatel), and a graphite rod comprising the three-electrode system were used as the working, reference, and counter electrodes, respectively. An alkaline electrolyte, 1 M potassium hydroxide (KOH) with 0.16 M potassium nitrate (KNO₃) was used

for the NO₃RR tests. The electrochemical cell was deaerated prior to electrochemical experiments by purging N₂ gas (research grade 99.9995% – PraxAir) for 30 min at 80 sscm. During the NO₃RR, N₂ gas was continuously purged at 30 sscm. Control experiments with only 1 M KOH + N₂ gas demonstrate that the catalyst is not active for N₂ reduction to NH₃, allowing N₂ to be an inert gas in this system (Figure S14a,b, Supporting Information). For the standard NO₃RR experiments, the working and counter electrolyte volumes were 30 and 25 mL, respectively. Chronoamperometric (CA) tests were performed for 15 min under vigorous stirring. Prior to CA measurements, the electrode was activated by a pre-reduction step at –1.5 V versus RHE for 90 s. Linear sweep voltammetry was performed by cathodically sweeping from 0.5 to –1.0 V versus RHE at a scan rate of 5 mV s^{–1}. Electrochemically active surface area (ECSA) was determined by varying the scan rate between 20–100 mV s^{–1} between 0.60–0.75 V versus RHE. For the 24-h durability test, which was segmented into eight, 3-h sections, an electrolyte reservoir of 250 mL was connected to the cathodic chamber of the H-cell using peristaltic pumps and was continually circulated throughout the electrolysis. The large circulating reservoir prevented the buildup of produced NH₃ from becoming too high in the cell. After a 3-h segment, all electrolyte was pumped back into the external reservoir, sampled, and then refreshed for the next 3-h segment. The potential reported for all electrochemical tests was not iR-corrected.

Isotopic (K¹⁵NO₃) Nitrate Reduction: To confirm the N in the detected NH₃ originated from the KNO₃ feed and not from the N-doped catalyst support, the N₂ gas or other sources of contamination, NO₃RR with isotopically doped K¹⁵NO₃ (99% – Cambridge isotopes) was performed. A 1 M KOH + 0.16 M K¹⁵NO₃ electrolyte was used. Isotopically labeled ¹⁵NO₃RR was performed at –1.0 V versus RHE for 15 min, after which the electrolyte was sampled and quantified by ¹H NMR. Isotopically doped ¹⁵NH₃ yielded a doublet and standard ¹⁴NH₃ resulted in a triplet.

Calculation of the Yield and FE: In this study, all error bars were reported based on a 90% confidence interval from a series of three independent measurements.

The yield rate of ammonia (*Yield*_{NH₃}) from the NO₃RR was calculated from Equation (2).

$$Yield_{NH_3} = \frac{c_{NH_3} \times V}{Mw_{NH_3} \times t \times A_{electrode}} \quad (2)$$

The FE for NH₃, *FE*_{NH₃}, was calculated from Equation (3).

$$FE_{NH_3} = \frac{n \times F \times c_{NH_3} \times V}{Mw_{NH_3} \times Q} \quad (3)$$

where *c*_{NH₃} is the concentration of NH₃ in the working chamber (mg mL^{–1}), *V* is the volume of the working chamber (30 mL), the molar mass of ammonia, *Mw*_{NH₃} is 17.031 g mol^{–1}, *t* is the electrolysis time (0.25 h), *A*_{electrode} is the area of the working electrode (0.25 cm²), *n* is the number of electrons transferred (8e[–] for NO₃[–] to NH₃), *F* is Faradays constant (96485 C), and *Q* is the charge passed during the electrolysis (C).

Product Detection: For typical NO₃RR tests, the detection and quantification of NH₃ was achieved using a UV–vis spectrophotometer (Shimadzu, UV-2600). NH₃ was detected using the indophenol blue method in which 2 mL of electrolyte (or diluted electrolyte) was mixed with 2 mL of solution A (1 M NaOH, 5 wt% salicylic acid, and 5 wt% sodium citrate), 1 mL of solution B (0.05 M NaClO), and solution C (1 wt% sodium nitro-ferricyanide). After incubating the dark at room temperature for 1 h, the maximum absorbance was taken at \approx 655 nm and quantified with respective calibration curves. Calibration curves for the detection and quantification of ¹⁴NH₃ were given in Figure S39, Supporting Information. It was noted that in certain instances, the *FE*_{NH₃} was over 100%. This was due to errors propagated during the dilution of the electrolyte. The electrolyte might be diluted such that the quantified NH₃ would fall within the calibration range. Given the ultrahigh yield rates in this work, dilutions up to 400× were employed.

For the detection of isotopic ammonia ($^{15}\text{NH}_3$), ^1H NMR was used. 3-(Trimethylsilyl)-1-propanesulfonic acid sodium salt (DSS) was selected as an internal standard and dimethylsulfoxide- d_6 (DMSO) was used as the locking solvent. The NMR spectra of a solution of 580 μL of electrolyte, 25 μL of DMSO, 20 μL of 3 M H_2SO_4 , and 75 μL of 6 mM DSS were obtained on a Bruker CRYO 500 MHz spectrometer. A solvent suppression method was applied to reduce the signal of H_2O , allowing for better resolution. The spectrum was processed using the Topspin 4.0.8 software. The linear calibration for the detection and quantification of $^{15}\text{NH}_3$ are given in Figure S40, Supporting Information.

Techno-Economic Analysis—Levelized Cost of Ammonia: To evaluate the trade-off between energy efficiency and ammonia partial current density, the levelized cost of ammonia (LC_{NH_3}) was employed as a metric. The LC_{NH_3} was calculated analogously to Daiyan et al. and was determined by Equation (4).^[22]

$$\text{LC}_{\text{NH}_3} = \frac{R_f \times \text{CAPEX} + \text{OPEX}}{\text{Yield}_{\text{NH}_3}} \quad (4)$$

where R_f is the capital recovery factor and is set at 0.08%. CAPEX was the capital cost and solely attributed to the cost of the electrolyzer stack (in \$). OPEX was the operational cost and constituted costs associated with electricity, nitrate feed, and water consumption (all in units of \$). $\text{Yield}_{\text{NH}_3}$ was the yield of ammonia (kg), giving a LC_{NH_3} in $\text{\$ kg}_{\text{NH}_3}^{-1}$. The $\text{Yield}_{\text{NH}_3}$ was calculated based as a function of the current density and electrolyzer area (with $8e^-$ transferred per NH_3).

The electrolyzer stack cost was based on parameters in analogous economic calculations and analysis provided in a National Renewable Energy Laboratory report with a cost of $\text{\$}342 \text{ kW}^{-1}$ operating at a cell voltage of 1.9 V and current density of 2 A cm^{-2} , which yielded an assumed NO_3RR electrolyzer stack cost of $12\,996 \text{ \$ m}^{-2}$.^[22,46] In the idealized case where the stack cost could be significantly reduced, a cost of $\text{\$}143 \text{ kWh}^{-1}$ was assumed, resulting in an electrolyzer cost of $5434 \text{ \$ m}^{-2}$. For the OPEX costs, the cost of the NO_3^- (NO_x) input was assumed to be $\text{\$}315$ per metric ton, as estimated in work by Jiang et al.^[22,47] The cost of water was assumed to be $\text{\$}0.02$ L and the cost of electricity from the grid was assumed to be $\text{\$}70 \text{ MWh}^{-1}$ and electricity generated from renewable sources was assumed to be $\text{\$}30 \text{ MWh}^{-1}$. The required electrolyzer area required was calculated from Equation (5).

$$A_{\text{electrolyzer}} = \frac{I_{\text{total}}}{j} \quad (5)$$

where I_{total} is the current passing through the electrode (A) and j is the current density of the NO_3RR system. I_{total} was determined by dividing the applied power to the stack (assumed here as 1 MW) by the cell voltage (assumed here as 1.9 V). Therefore, assuming a system current density of 1.3 A cm^{-2} (the performance demonstrated in the 24-h electrolysis), the total required electrolyzer area was 37.6 m^2 .

Supporting Information

Supporting Information is available from the Wiley Online Library or from the author.

Acknowledgements

This work is funded by the US Department of Energy, Office of Energy Efficiency and Renewable Energy (EERE), through the Advanced Manufacturing Office program to Sandia National Laboratories (SNL, AOP 34920). SNL is a multi-mission laboratory managed and operated by National Technology & Engineering Solutions of Sandia, LLC, a wholly-owned subsidiary of Honeywell International, Inc., for the US DOE's National Nuclear Security Administration under contract DE-NA-0003525. The views expressed in the article do not necessarily represent the views of the US

DOE or the United States Government. The authors acknowledge the use of facilities and instrumentation at the UC Irvine Materials Research Institute (IMRI), which is supported in part by the National Science Foundation through the UC Irvine Materials Research Science and Engineering Center (DMR-2011967). This work has been supported in part by the National Science Foundation (NSF) through the International Research Experiences for Students (IRES) program (NSF-2107534) Portions of this research were carried out at the P64 beamline at the DESY Synchrotron Radiation Facility, Hamburg, Germany, a member of the Helmholtz Association (HGF). The authors would like to thank Wolfgang Caliebe for his help in performing the in situ XAS measurements. Portions of this research were carried out at the SAMBA beamline at the SOLEIL Synchrotron Radiation Facility, Paris, France. The authors would like to sincerely thank the beamline scientists, Andrea Zitolo and Emiliano Fonda, for their help in performing the XAS measurements. The authors would like to thank Mingjie Xu for his assistance with STEM imaging in the revision process.

Conflict of Interest

The authors declare no conflict of interest.

Author Contributions

E.M. and B.S. contributed equally to this work. E.M.: Conceived the idea, designed and conducted experiments, processed and analyzed the data, and composed the original draft. B.S.: Designed and conducted experiments, and processed the data. M.R.: Performed ex situ and in situ XAS measurements, data analysis, and manuscript editing. Y.L.: Designed experiments and contributed to discussion and manuscript editing. W.Z.: Performed atomic resolution EELS measurements and analysis. S.G.: Assisted in experimental work, discussion, and manuscript editing. Y.C.: Performed durability experiments and STEM imaging for the revision process. U.H.: Performed ex situ and in situ XAS measurements data analysis. Y.H. and A.L.: Assisted in catalyst characterization and manuscript editing. I.V.Z. and X.P. supervised the study and contributed to discussions. J.T.: Supervised and performed ex situ and in situ XAS measurements data analysis and manuscript editing. B.R.C.: Supervised the study, funding acquisition, discussions, and manuscript editing. E.D.S.: Supervised the study, funding acquisition, discussions, and manuscript editing. P.A.: Conceived the idea, supervised the study, funding acquisition, and manuscript editing.

Data Availability Statement

The data that support the findings of this study are available from the corresponding author upon reasonable request.

Keywords

active support, alkaline, ammonia, in situ XAS, iron oxide, nitrate reduction, nitrite reduction, single atom catalysts

Received: January 22, 2024

Revised: March 22, 2024

Published online:

- [1] J. G. Chen, R. M. Crooks, L. C. Seefeldt, K. L. Bren, R. M. Bullock, M. Y. Darensbourg, P. L. Holland, B. Hoffman, M. J. Janik, A. K. Jones, M. G. Kanatzidis, P. King, K. M. Lancaster, S. V. Lyman, P. Pfromm, W. F. Schneider, R. R. Schrock, *Science* **2018**, 360, aar6611.

- [2] B. H. R. Suryanto, H. L. Du, D. Wang, J. Chen, A. N. Simonov, D. R. MacFarlane, *Nat. Catal.* **2019**, 2, 290.
- [3] H. Iriawan, S. Z. Andersen, X. Zhang, B. M. Comer, J. Barrio, P. Chen, A. J. Medford, I. E. L. Stephens, I. Chorkendorff, Y. Shao-Horn, *Nat. Rev. Methods Prim.* **2021**, 1, 56.
- [4] S. Z. Andersen, V. Čolić, S. Yang, J. A. Schwalbe, A. C. Nielander, J. M. McEnaney, K. Enemark-Rasmussen, J. G. Baker, A. R. Singh, B. A. Rohr, M. J. Statt, S. J. Blair, S. Mezzavilla, J. Kibsgaard, P. C. K. Vesborg, M. Cargnello, S. F. Bent, T. F. Jaramillo, I. E. L. Stephens, J. K. Nørskov, I. Chorkendorff, *Nature* **2019**, 570, 504.
- [5] J. Choi, B. H. R. Suryanto, D. Wang, H. L. Du, R. Y. Hodgetts, F. M. Ferrero Vallana, D. R. MacFarlane, A. N. Simonov, *Nat. Commun.* **2020**, 11, 5546.
- [6] P. H. van Langevelde, I. Katsounaros, M. T. M. Koper, *Joule* **2021**, 5, 290.
- [7] X. Liang, H. Zhu, X. Yang, S. Xue, Z. Liang, X. Ren, A. Liu, G. Wu, *Small Struct.* **2022**, 4, 2200202.
- [8] J. Sun, D. Alam, R. Daiyan, H. Masood, T. Zhang, R. Zhou, P. J. Cullen, E. C. Lovell, A. Jalili, *Energy Environ. Sci.* **2021**, 14, 865.
- [9] Z. Wang, D. Richards, N. Singh, *Catal. Sci. Technol.* **2021**, 11, 705.
- [10] F. Y. Chen, Z. Y. Wu, S. Gupta, D. J. Rivera, S. V. Lamberts, S. Pecaut, J. Y. T. Kim, P. Zhu, Y. Z. Finfrook, D. M. Meira, G. King, G. Gao, W. Xu, D. A. Cullen, H. Zhou, Y. Han, D. E. Perea, C. L. Muhich, H. Wang, *Nat. Nanotechnol.* **2022**, 17, 759.
- [11] S. Han, H. Li, T. Li, F. Chen, R. Yang, Y. Yu, B. Zhang, *Nat. Catal.* **2023**, 6, 402.
- [12] P. Li, Z. Jin, Z. Fang, G. Yu, *Energy Environ. Sci.* **2021**, 14, 3522.
- [13] J. Li, G. Zhan, J. Yang, F. Quan, C. Mao, Y. Liu, B. Wang, F. Lei, L. Li, A. W. M. Chan, L. Xu, Y. Shi, Y. Du, W. Hao, P. K. Wong, J. Wang, S. X. Dou, L. Zhang, J. C. Yu, *J. Am. Chem. Soc.* **2020**, 142, 7036.
- [14] Q. Hu, Y. Qin, X. Wang, Z. Wang, X. Huang, H. Zheng, K. Gao, H. Yang, P. Zhang, M. Shao, C. He, *Energy Environ. Sci.* **2021**, 14, 4989.
- [15] I. Katsounaros, *Curr. Opin. Electrochem.* **2021**, 28, 100721.
- [16] Y. Wang, A. Xu, Z. Wang, L. Huang, J. Li, F. Li, J. Wicks, M. Luo, D. H. Nam, C. S. Tan, Y. Ding, J. Wu, Y. Lum, C. T. Dinh, D. Sinton, G. Zheng, E. H. Sargent, *J. Am. Chem. Soc.* **2020**, 142, 5702.
- [17] L. Li, C. Tang, X. Cui, Y. Zheng, X. Wang, H. Xu, S. Zhang, T. Shao, K. Davey, S. Z. Qiao, *Angew. Chem., Int. Ed.* **2021**, 60, 14131.
- [18] J. Wang, C. Cai, Y. Wang, X. Yang, D. Wu, Y. Zhu, M. Li, M. Gu, M. Shao, *ACS Catal.* **2021**, 11, 15135.
- [19] W. He, J. Zhang, S. Dieckhöfer, S. Varhade, A. C. Brix, A. Lielpetere, S. Seisel, J. R. C. Junqueira, W. Schuhmann, *Nat. Commun.* **2022**, 13, 1129.
- [20] Z. Song, Y. Liu, Y. Zhong, Q. Guo, J. Zeng, Z. Geng, *Adv. Mater.* **2022**, 34, 2204306.
- [21] Z. Deng, C. Ma, Z. Li, Y. Luo, L. Zhang, S. Sun, Q. Liu, J. Du, Q. Lu, B. Zheng, X. Sun, *ACS Appl. Mater. Interfaces* **2022**, 14, 46595.
- [22] R. Daiyan, T. Tran-Phu, P. Kumar, K. Iputera, Z. Tong, J. Leverett, M. H. A. Khan, A. Asghar Esmailpour, A. Jalili, M. Lim, A. Tricoli, R. S. Liu, X. Lu, E. Lovell, R. Amal, *Energy Environ. Sci.* **2021**, 14, 3588.
- [23] F. Zhou, C. Sun, *Small* **2022**, 18, 2200436.
- [24] Z. Qiao, C. Wang, C. Li, Y. Zeng, S. Hwang, B. Li, S. Karakalos, J. Park, A. J. Kropf, E. C. Wegener, Q. Gong, H. Xu, G. Wang, D. J. Myers, J. Xie, J. S. Spendlow, G. Wu, *Energy Environ. Sci.* **2021**, 14, 4948.
- [25] A. Ly, H. Wang, E. Murphy, Y. Huang, S. Guo, Y. Liu, I. V. Zenyuk, P. Atanassov, *ECS Meet. Abstr.* **2022**, MA2022-01, 1472.
- [26] X. Ao, W. Zhang, B. Zhao, Y. Ding, G. Nam, L. Soule, A. Abdelhafiz, C. Wang, M. Liu, *Energy Environ. Sci.* **2020**, 13, 3032.
- [27] E. Murphy, Y. Liu, I. Matanovic, S. Guo, P. Tieu, Y. Huang, A. Ly, S. Das, I. Zenyuk, X. Pan, E. Spoecker, P. Atanassov, *ACS Catal.* **2022**, 12, 6651.
- [28] E. Murphy, Y. Liu, I. Matanovic, Y. Huang, A. Ly, S. Guo, W. Zang, X. Yan, I. Zenyuk, E. Spoecker, A. Plamen, *Nat. Commun.* **2023**, 2, 4.
- [29] Z. Wu, M. Karamad, X. Yong, Q. Huang, D. A. Cullen, P. Zhu, C. Xia, Q. Xiao, M. Shakouri, F. Chen, J. Y. Kim, Y. Xia, K. Heck, Y. Hu, M. S. Wong, Q. Li, I. Gates, S. Siahrostami, H. Wang, *Nat. Commun.* **2021**, 12, 2870.
- [30] H. Tan, J. Verbeeck, A. Abakumov, G. Van Tendeloo, *Ultramicroscopy* **2012**, 116, 24.
- [31] L. Liang, H. Jin, H. Zhou, B. Liu, C. Hu, D. Chen, Z. Wang, Z. Hu, Y. Zhao, H. W. Li, D. He, S. Mu, *Nano Energy* **2021**, 88, 106221.
- [32] J. Gao, X. Zhou, Y. Wang, Y. Chen, Z. Xu, Y. Qiu, Q. Yuan, X. Lin, H. J. Qiu, *Small* **2022**, 18, 2202071.
- [33] F. Wang, X. Liu, B. Jiang, H. Zhuo, W. Chen, Y. Chen, X. Li, *J. Colloid Interface Sci.* **2023**, 635, 514.
- [34] G. Greczynski, L. X.-R. P. S. Hultman, *Prog. Mater. Sci.* **2020**, 107, 100591.
- [35] A. Situm, X. Guo, B. C. Barlow, B. Guo, I. J. Burgess, A. P. Grosvenor, *Corros. Sci.* **2018**, 145, 35.
- [36] A. Martini, E. Borfecchia, *Crystals* **2020**, 10, 664.
- [37] J. Timoshenko, F. T. Haase, S. Saddeler, M. Rüscher, H. S. Jeon, A. Herzog, U. Hejral, A. Bergmann, S. Schulz, B. Roldan Cuenya, *J. Am. Chem. Soc.* **2022**, 145, 4065.
- [38] J. Timoshenko, A. I. Frenkel, *ACS Catal.* **2019**, 9, 10192.
- [39] A. Martini, E. Borfecchia, K. A. Lomachenko, I. A. Pankin, C. Negri, G. Berlier, P. Beato, H. Falsig, S. Bordiga, C. Lamberti, *Chem. Sci.* **2017**, 8, 6836.
- [40] J. Jaumot, R. Gargallo, A. De Juan, R. Tauler, *Chemom. Intell. Lab. Syst.* **2005**, 76, 101.
- [41] J. Li, A. Zitolo, F. A. Garcés-Pineda, T. Asset, M. Kodali, P. Tang, J. Arbiol, J. R. Galán-Mascarós, P. Atanassov, I. V. Zenyuk, M. T. Sougrati, F. Jaouen, *ACS Catal.* **2021**, 11, 10028.
- [42] C. Genovese, M. E. Schuster, E. K. Gibson, D. Gianolio, V. Posligua, R. Grau-Crespo, G. Cibin, P. P. Wells, D. Garai, V. Solokha, S. Krick Calderon, J. J. Velasco-Velez, C. Ampelli, S. Perathoner, G. Held, G. Centi, R. Arrigo, *Nat. Commun.* **2018**, 9, 935.
- [43] K. M. Wagner, T. Karathanasis, C. J. Matocha, *Water* **2022**, 14, 2796.
- [44] W. Teng, N. Bai, Y. Liu, Y. Liu, J. Fan, W. X. Zhang, *Environ. Sci. Technol.* **2018**, 52, 230.
- [45] L. Lin, H. Li, Y. Wang, H. Li, P. Wei, B. Nan, R. Si, G. Wang, X. Bao, *Angew. Chem., Int. Ed.* **2021**, 133, 26786.
- [46] J. Vicker, D. Peterson, K. Randolph, *Department Energy United States Am.* **2020**, 5.
- [47] K. Jiang, H. Yu, L. Chen, M. Fang, M. Azzi, A. Cottrell, K. Li, *Appl. Energy* **2020**, 260, 114316.